



Article

Urban Heat Island Assessment Using the Landsat 8 Data: A Case Study in Shenzhen and Hong Kong

Jinyeu Tsou¹, Jing Zhuang¹, Yu Li² and Yuanzhi Zhang^{1,3,*}

¹ Center for Housing Innovations, The Chinese University of Hong Kong, Shatin, New Territories, Hong Kong, China; jinyeutsou@cuhk.edu.hk (J.T.); jingzhuang@link.cuhk.edu.hk (J.Z.)

² Faculty of Information Technology, Beijing University of Technology, Beijing 100124, China; yuli@bjut.edu.cn

³ Key Lab of Lunar Science and Deep-Space Exploration, Chinese Academy of Sciences, Beijing 100012, China

* Correspondence: yuanzhizhang@cuhk.edu.hk; Tel.: +86-10-6480-7833

Academic Editor: Matheos Santamouris

Received: 11 January 2017; Accepted: 16 March 2017; Published: 20 March 2017

Abstract: In this study, we assess the urban heat island (UHI) effect using remote sensing data, a phenomenon emerging under the background of global warming and urbanization. With the rapid development of satellite technology, remote sensing images are widely applied to evaluate the UHI effect on rapidly-urbanized areas in recent years. In the study, we applied Landsat 8 data to estimate the land surface temperature (LST) in the case study of Shenzhen and Hong Kong. The methods of the mono-window algorithm (MWA), single-channel method (SCM), Qin's split-window algorithm (SWA-Q) and Sobrino's split-window algorithm (SWA-S) are used to calculate the LST from Landsat 8 data on 29 November 2013, 16 November 2014, 18 October 2015, and 7 February 2016. The results show that LST retrievals by SWA-Q are better than those of the other algorithms in the case study of Shenzhen and Hong Kong. From 2013 to 2016, the high-LST zones or UHIs in Shenzhen and Hong Kong are substantially identical. Although the LST is not obviously correlated with vegetation distribution, the growth condition of vegetation may impact the distribution of the UHI, and the high LST is slightly correlated to the high atmospheric particulate concentration. Additionally, in general, Shenzhen and Hong Kong are weak UHI regions and the UHI-affected area in Shenzhen is larger than that in Hong Kong from 2013 to 2016.

Keywords: urban heat island; land surface temperature; Landsat 8; mono-window algorithm; single-channel method; split-window algorithm

1. Introduction

The urban heat island (UHI) effect is a phenomenon that the land surface temperature in urban areas is apparently higher than that in rural areas [1]. The causes of UHI are diverse, including natural factors and human factors, whose root cause is the change of land use. Additionally, the factors such as urban configuration, heat release from anthropogenic heat source, atmospheric pollution, geographic location, and climate also affect the UHI [2]. With the development of urbanization, urban built-up areas, namely, impervious surfaces, including roads and buildings, instead of green lands and water bodies, are rapidly sprawling and, thus, the city will suffer from the UHI effect [3]. Shenzhen, a main financial center in Southern China, increased its urban areas from around 3.06% to 39.3% from 1986 to 2005 [4]; Hong Kong is a metropolis with a high population density filled with high-rise buildings and has a lack of public open spaces in urban areas [5]; therefore, the urban areas in Shenzhen and Hong Kong suffer from a severe UHI effect.

The traditional method for UHI study relies on meteorology data derived from urban and rural weather stations. It is difficult to obtain abundant meteorology data and impossible to acquire surface meteorology data, aside from dotted meteorology data [6,7]. After the launch of the first

artificial Earth satellite, Sputnik, in 1957, satellite images have been widely applied in various fields. The satellite images with a thermal infrared band, such as the images of Landsat TM, Landsat OLI, ASTER (Advanced Spaceborne Thermal Emission and Reflection Radiometer) and MODIS (Moderate Resolution Imaging Spectroradiometer), can be converted to land surface temperature (LST) to study the UHI. In 1972, Rao firstly proposed that remote sensing could be applied to study the UHI and produced a land surface thermal distribution graph by the thermal infrared data from satellite images [8,9]. After that, satellite images have been widely used to study the LST and UHI. Therefore, various algorithms, such as the mono-window algorithm (MWA), single-channel method (SCM) and split-window algorithm (SWA) were proposed for LST estimation.

Howard firstly discovered the temperature in the center of London was obviously higher than that in its suburbs [10,11]. In China, the LST and land use classification were first applied in Guangzhou, China using the Landsat TM data from 1985 to 2000 to compare the correlation between the UHI and land use types, and suggested that the urban greening and landscape designs in Guangzhou should consider more about vegetation types, namely forest, shrubs, and lawns, to control the UHI [12]. In Canada, the temperature difference among different land use types in Toronto on 3 September 2008 using the Landsat TM data discovered that the higher urban utilization corresponded to higher UHI intensity [13]. Recently, the correlations among UHI intensity index, normalized difference vegetation index (NDVI), normalized difference water index (NDWI), and difference vegetation index (DVI) from Landsat TM data were used in Beijing, and the results show that if the UHI intensity index was less than 0.1, the correlation between the UHI intensity index and DVI was positive, and vice versa [14]. In addition, the UHI intensity of Seoul, Tokyo, and Beijing from April 2011 to March 2012 using the Communication, Ocean, and Meteorological Satellite (COMS) data was studied and compared to discover that the UHI intensity was strongest at noon during summer and weakest at night during all seasons, and the correlation between UHI intensity and vegetation activity was strongly negative during the day, but no such correlation existed during the night [15].

The MWA was applied to convert the LST in the Israel-Egypt border area using the Landsat TM data and discovered that although the vegetation coverage in Israeli side was higher than that on the Egyptian side, the LST on the Israeli side was higher than that of the Egyptian side [16]. This method was examined to derive the LST in Hong Kong using the Landsat TM data and then estimated the UHI by NDVI, normalized difference build-up index (NDBI), and urban thermal field variance index (UTFVI) [17]. In addition, an improved MWA was developed to estimate the LST using Landsat 8 band 10 and applied to retrieve the LST in Nanjing and its surrounding areas in Eastern China [18]. The MWA was also used to retrieve the LST in Xuzhou in Jiangsu, China from Landsat 8 data and then applied the urban land surface moisture (ULSM) index to evaluate the UHI in Xuzhou and found that an area with high ULSM had a cooling effect on its surrounding area within 150 m [19].

SCM was applied to estimate LST in that it did not need in situ radio soundings and mean atmospheric temperature compared with other SCMs to evaluate the LST using data of different thermal sensors, including AVHRR-4, AVHRR-5, ATSR2-11, ATSR2-12, and Landsat TM [20]. Later on, an improved SCM was developed to adopt five different atmospheric sounding datasets to derive the atmospheric functions and applied to convert the LST in Barrax, Albacete in Spain using the Landsat TM data [21]. This method was recently applied to convert the LST in Shenzhen, China using Landsat 5 TM data, and indicated that the LST had a negative correlation with the vegetation fraction and a positive correlation with the impervious surface area [22]. It is said that the SCM can be used to convert the LST in several study sites using the Landsat 8 data, comparing the satellite-derived LST results with the in situ LST results, with a high accuracy of the root mean square error (RMSE) of 0.83 °C [23].

In addition, the LST can be estimated using AVHRR data via an SWA which only needs two parameters, namely, the atmospheric transmittance and land surface emissivity, improving the accuracy to 0.24 °C [24]. This means that SWA could be applied to retrieve the LST using several low-resolution thermal infrared sensors data. Although the precision of this method was not very high, it was convenient to apply at a global scale [25]. It is reported that this method improved the accuracy of an

SWA via parameter adjustment, including the atmospheric transmittance, land surface emissivity, and water vapor content, and finally decreased the RMSE to 0.9 °C [26]. In recent years, a practical SWA was developed to convert the LST in Taiyuan-Yuci, China using the Landsat 8 data and improved the RMSE to 0.51 °C [27].

In most studies, SWA and SCM were applied and compared to derive the LST using Landsat 8 data and illustrated that the mean errors of both SWA and SCM were lower than 1.5 °C, while the precision of SWA was slightly higher than the SCM [28]. However, when the radiative transfer equation-based method (RTEBM), SWA, and SCM were applied to assess the LST using Landsat 8 data and compared the accuracy among these three methods, it is found that the accuracy of these three methods in descending order was the RTEBM, SWA, and SCM [29]. In addition, a practical SWA was applied to retrieve the LST in urban area of Beijing and Gobi, China using the Landsat 8 data, and it was found that the precision of the practical SWA, lower than 1.0 °C, is the best method [30].

Although there are a large number of studies to estimate LST using Landsat data, there has been few reports of Landsat 8 data being applied to the comparison of the difference and similarity of LST and assessing UHI in Shenzhen and Hong Kong. This study presents the UHI assessment using Landsat 8 as a case study in Shenzhen and Hong Kong.

2. Study Area

Shenzhen (SZ) is located in Southern China, to the east of the Pearl River Estuary and the northern coast of South China Sea, and constitutes 10 districts, namely, Guangming, Baoan, Longhua, Nanshan, Futian, Longgang, Luohu, Pingshan, Yantian, and Dapeng (Figure 1) [31]. It is a modern city with rapid economic development in Guangdong Province, China, whose population was approximately 10,778,900 in 2014, and has a total area of approximately 1992 km² [32].

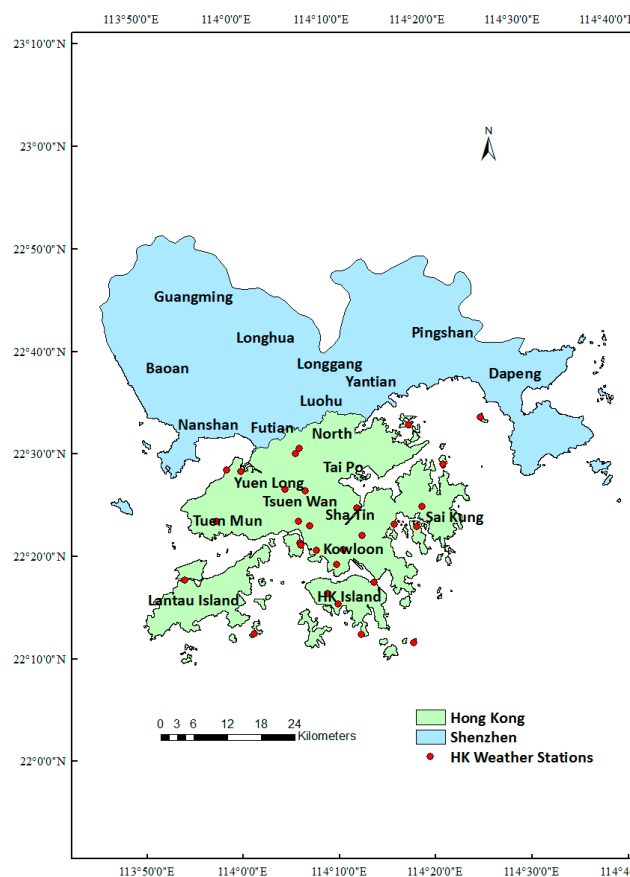


Figure 1. The map of Hong Kong and Shenzhen.

Hong Kong (HK) is located in the south of Shenzhen and comprises of Hong Kong Island, Kowloon and New territories, including 18 districts, namely, the islands of Kwai Tsing, North, Sai Kung, Sha Tin, Tai Po, Tsuen Wan, Tuen Mun, Yuen Long, Kowloon City, Kwun Tong, Sham Shui Po, Wong Tai Sin, Yau Tsim Mong, Central and Western, Eastern, Southern, and Wan Chai (Figure 1) [31]. It is one of the most significant financial centers in the world, whose population was approximately 7,324,300 at the end of 2015, and has a total area of around 1110 km² [33,34].

3. Materials and Methods

3.1. Materials

Four satellite images from Landsat 8 on 29 November 2013, 16 November 2014, 18 October 2015, and 7 February 2016, respectively, were delivered by the United States Geological Survey (USGS) [35]. All of them are acquired in winter and have less cloud cover in the whole image, and no apparent cloud cover in the study areas of this paper (Table 1).

Table 1. The information of the satellite images.

Satellite	Sensor ID	Pixel Size (m)	Cloud (%)	Date	Scene Center Time
Landsat 8	OLI and TIRS	30	3.46	29 November 2013	02:53:44.0940717Z
			8.90	16 November 2014	02:52:19.6126999Z
			1.15	18 October 2015	02:52:08.6842752Z
			2.63	7 February 2016	02:52:07.9603863Z

The vector maps of Shenzhen and Hong Kong were downloaded from DIVA-GIS for the geometric correction and image clip in image pre-processing, and the final map was exported with ArcGIS 10.1 software provided by ESRI (Environmental Systems Research Institute, Inc., Redlands, CA, USA) [36]. Then, satellite images were preprocessed before the LST conversion: firstly, satellite images of various bands were combined together with the layer stacking tool in ENVI 5.1 software provided by ESRI; secondly, the vector maps of Shenzhen and Hong Kong were subjected to geometric correction and image clip with subset data via the ROIs tool in ENVI 5.1 (Figure 1) [17].

The meteorology data on 29 November 2013, 16 November 2014, 18 October 2015, and 7 February 2016 from the weather stations in Shenzhen and Hong Kong, including the mean daily temperature and mean daily relative humidity were, respectively, collected from Weather Website and Hong Kong Observatory and utilized to calculate the mean atmospheric temperature and water vapor content for the LST conversion. Additionally, the latitude and longitude of 28 Hong Kong weather stations were utilized to extract the weather stations' LST for the final export [37,38].

3.2. Methods

The MWA, SCM, SWA-Q, and SWA-S were applied to retrieve the LST in Shenzhen and Hong Kong using the Landsat 8 data with ENVI 5.1, as elaborated in the following.

3.2.1. Mono-Window Algorithm

The MWA converts the LST using Landsat 8 band 10 via the parameter calculation, including the mean atmospheric temperature, brightness temperature, atmospheric transmittance, and land surface emissivity, as Equations (1)–(3) [18]:

$$T_s = (a_{10}(1 - C_{10} - D_{10}) + [b_{10}(1 - C_{10} - D_{10}) + C_{10} + D_{10}]T_{10} - D_{10}T_a) / C_{10} \quad (1)$$

$$C_i = \tau_i \varepsilon_i \quad (2)$$

$$D_i = (1 - \tau_i)[1 + (1 - \varepsilon_i)\tau_i] \quad (3)$$

where T_s is the LST (K); a_{10} and b_{10} are constants (Table 2) [26]; C_i and D_i are the parameters of band i ; T_a is the mean atmospheric temperature (K); T_{10} is the brightness temperature (K) of band 10; τ_i is the atmospheric transmittance of band i ; ε_i is the land surface emissivity of band i . According to the suggestion from USGS, Landsat 8 band 10 is more accurate than band 11 and, therefore, the data of band 10 are utilized in the MWA and SCM, which only need one infrared band to convert the LST [18].

Table 2. The coefficient value for Landsat 8 (the temperature of study areas ranges between 10 and 40 °C and the coefficient value at this temperature range using Equation (1)).

Temperature Range (°C)	a_{10}	b_{10}	a_{11}	b_{11}
10–40	−62.8065	0.4338	−67.1728	0.4694

The brightness temperature is the temperature of black body which is same as the temperature of an actual object in the same wavelength computed by the following two steps [32]: firstly, calculating the spectral radiance using the digital numbers (DNs) of thermal infrared bands, namely Landsat 8 band 10 or 11, as Equation (4); and, secondly, computing the brightness temperature using spectral radiance by Equation (5) [18]:

$$R_i = M_i Q_i + A_i \quad (4)$$

$$T_i = \frac{K_2}{\ln(1 + K_1/R_i)} \quad (5)$$

where R_i is the spectral radiance ($\text{W}\cdot\text{m}^{-2}\cdot\text{sr}^{-1}\cdot\mu\text{m}^{-1}$) of band i ; M_i is the band-specific multiplicative rescaling factor for band i ; Q_i is the DN of band i ; A_i is the band-specific additive rescaling factor for band i ; T_i is the brightness temperature (K) of band i ; K_1 and K_2 are the thermal conversion constants (Table 3). In addition, M_i , A_i , K_1 , and K_2 are constants that are acquired from the documents enclosed with the downloaded Landsat 8 data.

Table 3. The constant values of Landsat 8 band 10 and 11.

Bands	Constants			
	M_i	M_i	K_1 ($\text{W}\cdot\text{m}^{-2}\cdot\text{sr}^{-1}\cdot\mu\text{m}^{-1}$)	K_2 (K)
Band 10	0.0003342	0.1	774.8853	1321.0789
Band 11			480.8883	1201.1442

The mean atmospheric temperature is the average temperature at different levels of the Earth's atmosphere was computed by the following two steps [32]: firstly, converting the observed temperature from weather stations into the air temperature in the recording time of satellite images (Table 1) by Equation (6) [18,39]; secondly, because both Shenzhen and Hong Kong are located in tropical areas, the mean atmospheric temperature is calculated using the station air temperature by Equation (7) [16]:

$$T_{0,t} = T_{\tau\min} + (T_{\tau\max} - T_{\tau\min}) \sin[\pi(t + \frac{t_{dl}}{2} - 12)/(t_{dl} + 2t_{\tau\max})] \quad (6)$$

$$T_a = 17.9769 + 0.9172T_0 \quad (7)$$

where $T_{0,t}$ is the station air temperature (K) at time t (Table 1); $T_{\tau\min}$ and $T_{\tau\max}$ are, respectively, the daily minimum and maximum air temperature (K); t_{dl} is the day length (h); $t_{\tau\max}$ is the time difference between local solar noon and time of $T_{\tau\max}$; T_a is the mean atmospheric temperature (K); and T_0 is the station air temperature (K).

The water vapor content, which is computed by Equations (8) and (9), is used to choose the atmospheric transmittance formulas [18]. In this paper, the water vapor content is 0.2–3.0 g/cm², so the special atmospheric transmittance formulas of band 10 and 11 are presented in Table 4 [29]:

$$\omega = \omega(0)/R_\omega(0) \tag{8}$$

$$\omega(0) = H \times E \times a/1000 \tag{9}$$

where ω is the total water vapor content (g/cm²); $\omega(0)$ is the water vapor content (g/cm²) at ground level; $R_\omega(0)$ is the ratio of water vapor content at the first layer to the total, and for tropical atmosphere, $R_\omega(0) = 0.6834$; H is the relative humidity (%); E is the saturation mix ratio (g/kg) of water vapor and air; a is the air density (g/m³) (Table 5). According to the meteorology data in Shenzhen and Hong Kong, the average of weather stations' mean daily air temperatures are approximately 15 °C on both 29 November 2013 and 7 February 2016 and, therefore, the related values for the water vapor content calculation are collected in Table 5.

Table 4. The atmospheric transmittance formulas from the 1976 US standard.

Water Vapor Content (g/cm ²)	Atmospheric Transmittance Formulas
0.2–3.0	$\tau_{10} = -0.01646\omega^2 - 0.04546\omega + 0.9744$ $\tau_1 = -0.01403\omega^2 - 0.09748\omega + 0.9731$

Table 5. The values of saturation mix ratio and air density.

T (°C)	E (g/kg)	a (kg/m ³)
15	10.83	1.23

The land surface emissivity of band 10 or 11 is classified by the normalized difference vegetation index (NDVI), which can extract vegetation from soil and water, as Equations (10)–(13) [18,40]:

$$\varepsilon_i = \begin{cases} \varepsilon_{s\lambda i}, & NDVI < NDVI_s \\ \varepsilon_{s\lambda i}P_v + \varepsilon_{s\lambda i}(1 - P_v) + C_{\lambda i}, & NDVI_s \leq NDVI \leq NDVI_v \\ \varepsilon_{s\lambda i}P_v + C_{\lambda i} & NDVI > NDVI_v \end{cases} \tag{10}$$

$$NDVI = \frac{NIR - R}{NIR + R} \tag{11}$$

$$P_v = \left[\frac{NDVI - NDVI_s}{NDVI_v - NDVI_s} \right]^2 \tag{12}$$

$$C_{\lambda i} = (1 - \varepsilon_{s\lambda i})\varepsilon_{v\lambda i}F'(1 - P_v) \tag{13}$$

where ε_i is the land surface emissivity of band i ; $\varepsilon_{s\lambda i}$ and $\varepsilon_{v\lambda i}$ are, respectively, the soil and vegetation emissivity of band i (Table 6) [27]; P_v is the proportion of vegetation ranging between 0 and 1; $C_{\lambda i}$ is the surface roughness of band i ; $NDVI_s$ and $NDVI_v$ are, respectively, the NDVI for soil and vegetation and, generally, $NDVI_s = 0.2$, $NDVI_v = 0.5$, but $NDVI_v$ would be higher in dense vegetation areas, so $NDVI_v = 0.8$ in this study; NIR is the near-infrared band; R is the red band; and F' is a geometrical factor ranging between 0 and 1 and, generally, $F' = 0.5$.

Table 6. The emissivity of soil and vegetation for Landsat 8 band 10 and 11.

Bands	Emissivity	
	$\epsilon_{s\lambda i}$	$\epsilon_{v\lambda i}$
Band 10	0.964	0.984
Band 10	0.970	0.980

3.2.2. Single-Channel Method

The SCM retrieves the LST based on the calculation of the spectral radiance and brightness temperature of Landsat 8 band 10, total water vapor content and land surface emissivity etc., as Equations (14)–(19) [28]:

$$T_s = \gamma \left[\frac{1}{\epsilon_{10}} (\psi_1 R_{10} + \psi_2) + \psi_3 \right] + \delta \quad (14)$$

$$\gamma \approx \frac{\tau_{10}^2}{b_\gamma R_{10}} \quad (15)$$

$$\delta \approx T_{10} - \frac{\tau_{10}^2}{b_\gamma} \quad (16)$$

$$\psi_1 = 0.04019\omega^2 + 0.02916\omega + 1.01523 \quad (17)$$

$$\psi_2 = -0.38333\omega^2 - 1.50294\omega + 0.20324 \quad (18)$$

$$\psi_3 = 0.00918\omega^2 + 1.36072\omega - 0.27514 \quad (19)$$

where T_s is the LST (K); γ and δ are parameters; ϵ_{10} is the land surface emissivity of band 10 obtained; ψ_1 , ψ_2 and ψ_3 are the atmospheric functions; R_{10} is the spectral radiance ($\text{W} \cdot \text{m}^{-2} \cdot \text{sr}^{-1} \cdot \mu\text{m}^{-1}$) of band 10; T_{10} is the brightness temperature (K) of band 10; for band 10, $b_\gamma = 1324\text{K}$; and ω is the total water vapor content (g/cm^{-2}).

3.2.3. Qin's Split-Window Algorithm

The SWA-Q derives the LST using Landsat 8 band 10 and 11 via parameter calculation, including the total water vapor content, brightness temperature, atmospheric transmittance, and land surface emissivity of band 10 and 11, as Equations (20)–(27) [24,26]:

$$T_s = A_0 + A_1 T_{10} - A_2 T_{11} \quad (20)$$

$$A_0 = E_1 a_{10} + E_2 a_{11} \quad (21)$$

$$A_1 = 1 + A + E_1 b_{10} \quad (22)$$

$$A_2 = A + E_2 b_{11} \quad (23)$$

$$E_1 = D_{11}(1 - C_{10} - D_{10})/E_0 \quad (24)$$

$$E_2 = D_{10}(1 - C_{11} - D_{11})/E_0 \quad (25)$$

$$E_0 = D_{11}C_{10} - D_{10}C_{11} \quad (26)$$

$$A = D_{10}/E_0 \quad (27)$$

where T_s is the LST (K); T_{10} and T_{11} are respectively the brightness temperature of band 10 and 11; $A_0, A_1, A_2, E_1, E_2, E_0$, and A are parameters; C_i and D_i are the parameters of band i ; a_{10}, a_{11}, b_{10} , and b_{11} are coefficients (Table 2) [26].

3.2.4. Sobrino's Split-Window Algorithm

The SWA-S estimates the LST using Landsat 8 band 10 and 11 by parameter computation, including the total water vapor content, brightness temperature, and land surface emissivity of band 10 and 11, as Equations (28)–(30) [25,28]:

$$T_s = T_{10} + c_1(T_{10} - T_{11}) + c_2(T_{10} - T_{11})^2 + c_0 + (c_3 + c_4\omega)(1 - \varepsilon) + (c_5 + c_6\omega)\Delta\varepsilon_r \quad (28)$$

$$\varepsilon = (\varepsilon_{10} + \varepsilon_{11})/2 \quad (29)$$

$$\Delta\varepsilon = \varepsilon_{10} - \varepsilon_{11} \quad (30)$$

where T_s is the LST (K); T_{10} and T_{11} are, respectively, the brightness temperature of band 10 and 11; $c_0, c_1, c_2, c_3, c_4, c_5$, and c_6 are coefficients (Table 7) [28]; ω is the total water vapor content (g/cm^{-2}); ε is the mean land surface emissivity; $\Delta\varepsilon$ is the land surface emissivity difference; and ε_{10} and ε_{11} are, respectively, the land surface emissivity of band 10 and 11.

Table 7. The coefficient values for SWA-S.

c_0	c_1	c_2	c_3	c_4	c_5	c_6
−0.268	1.378	0.183	54.30	−2.238	−129.20	16.40

3.3. Objective and Processing

The objective of this paper is summarized as follows:

- Accuracy comparison of four LST conversion methods, namely, the MWA, SCM, Qin's split-window algorithm (SWA-Q), and Sobrino's split-window algorithm (SWA-S);
- Analysis of the LST and UHI for Shenzhen and Hong Kong in 2013, 2014, 2015, and 2016 after the estimation of the LST and UHI for Shenzhen and Hong Kong.

The processing of this study (Figure 2):

- Data collection and image pre-processing, including the Landsat 8 data, vector maps, and meteorology data of Shenzhen and Hong Kong;
- The LST simulation of Shenzhen and Hong Kong by the MWA, SCM, SWA-Q and SWA-S;
- Analysis, including the accuracy of four methods, simulation error, and difference in LST and UHI between Shenzhen and Hong Kong from 2013 to 2016;
- Comparison of this study with others.

The flowchart of this study is provided in Figure 2:

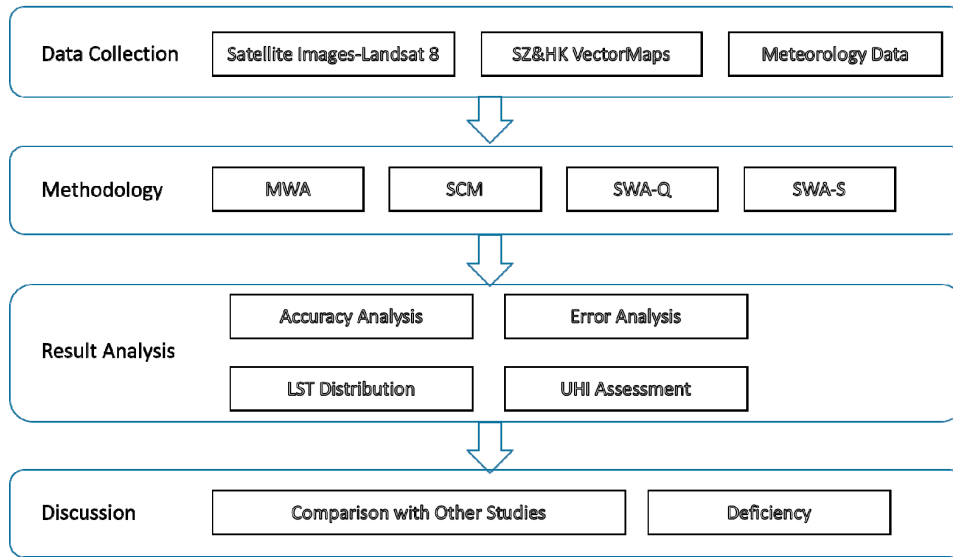


Figure 2. Data processing flowchart.

4. Results

According to the LST retrievals via MWA, SCM, SWA-Q, and SWA-S, the further analysis, including the accuracy analysis, error analysis, LST distribution, and UHI assessment of Shenzhen and Hong Kong, is presented in the following.

4.1. Accuracy Assessment

For comparing the accuracy of four methods, and then selecting the most accurate method to analyze the LST and UHI in Shenzhen and Hong Kong, the LST retrievals from 28 Hong Kong weather stations are extracted to compare with the mean daily air temperature collected from the Hong Kong Observatory (Figures 3–6) [38].

From Figures 3–6, T_s is the LST (°C); T is the mean daily air temperature (°C); R is correlation coefficient; p is p -value; and k is linear slope. In Figure 3, the distribution of LST retrieval is more scattered than that of the mean daily air temperature, that is to say, the LST retrieval has some extreme values that decrease the general accuracy. In addition, the range of SWA-Q’s LST retrieval, basically between 10.0 °C and 20.0 °C, is relatively closer to the range of the measured mean air temperature, approximately between 12.0 °C and 16.0 °C, compared with the range of the other three methods’ LST retrievals, mostly between 15.0 °C and 25.0 °C.

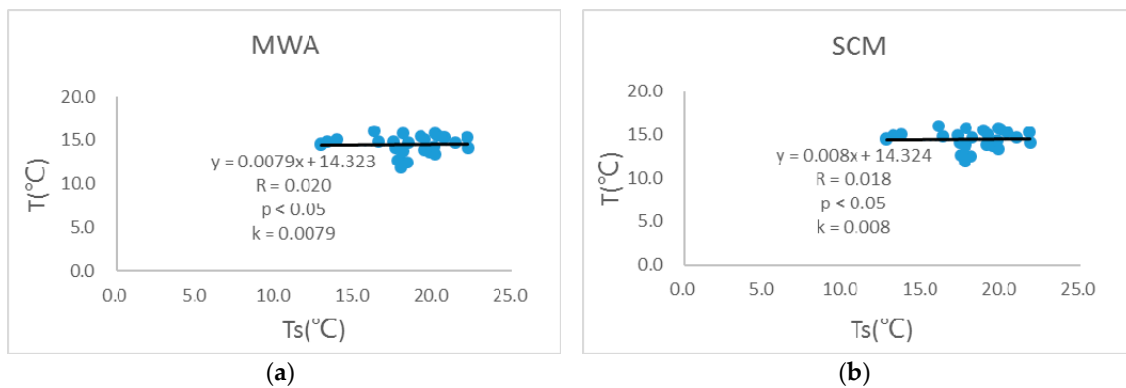


Figure 3. Cont.

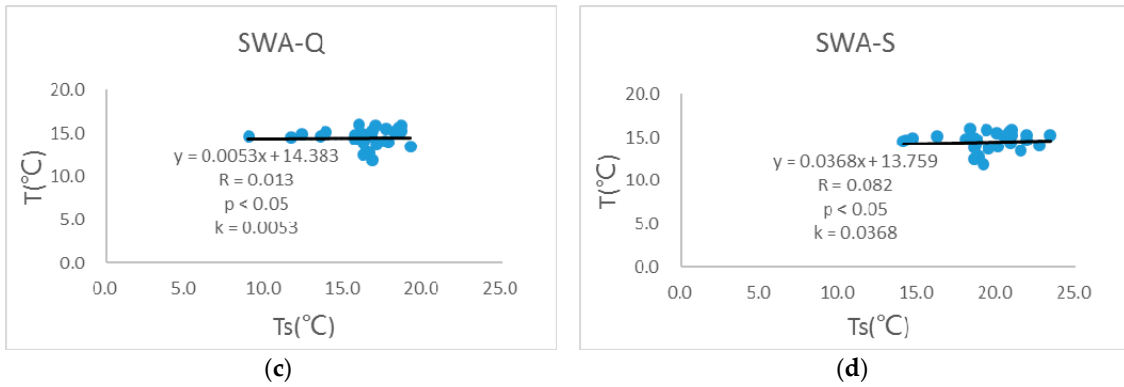


Figure 3. The scatterplots of the LST retrievals by the (a) MWA; (b) SCM; (c) SWA-Q; and (d) SWA-S compared with the mean daily air temperature in 29 November 2013.

In Figure 4, the distribution of LST retrieval is more concentrated than that in Figure 3, in other words, the LST retrieval in Figure 4 has fewer extreme values than that in Figure 3. Additionally, the range of SWA-Q’s LST retrieval, basically between 20.0 °C and 29.0 °C, is relatively closer to the range of measured mean air temperature, approximately between 20.0 °C and 23.0 °C, compared with the range of the other three methods’ LST retrievals, mostly between 22.0 °C and 33.0 °C.

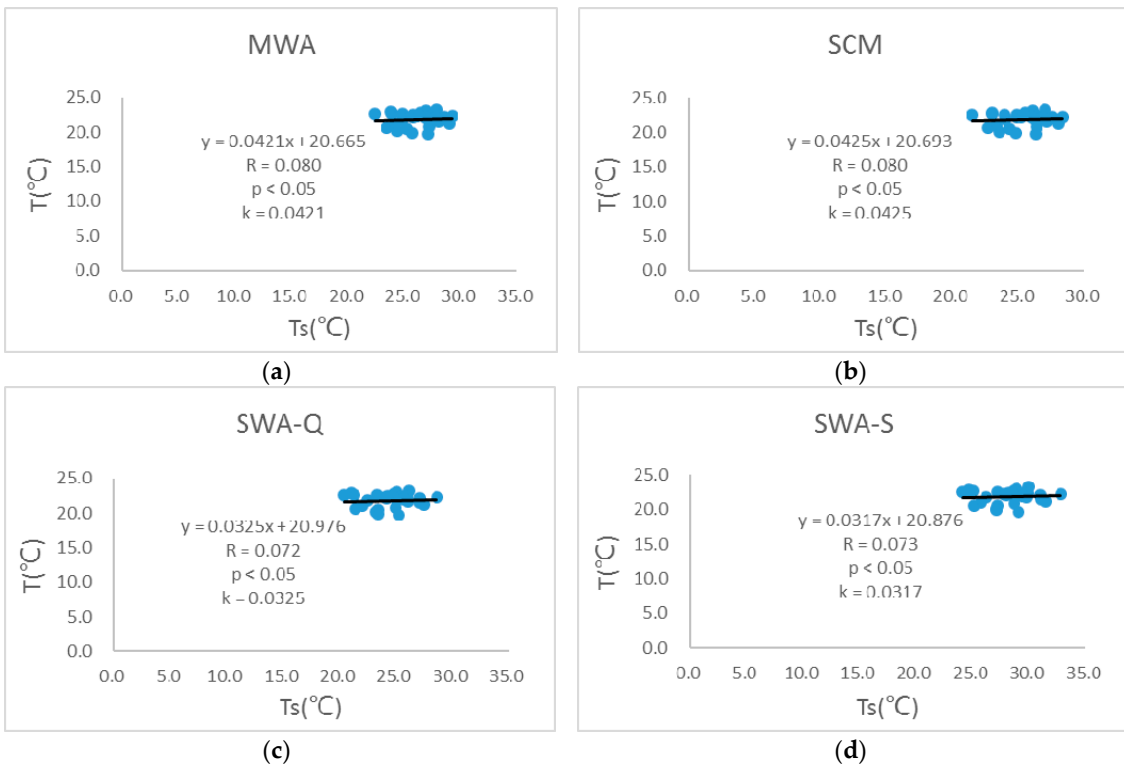


Figure 4. The scatterplots of the LST retrievals by the (a) MWA; (b) SCM; (c) SWA-Q; and (d) SWA-S compared with the mean daily air temperature in 16 November 2014.

In Figure 5, the distribution of LST retrieval is much more scattering than that of the mean daily air temperature and has an extremely low value which may influence the LST’s accuracy. Additionally, the range of the SWA-Q’s LST retrieval, basically between 21.0 °C and 31.0 °C, is relatively closer to the range of measured mean air temperature, approximately between 21.0 °C and 26.0 °C, compared with the range of the other three methods’ LST retrievals, mostly between 23.0 °C and 34.0 °C.

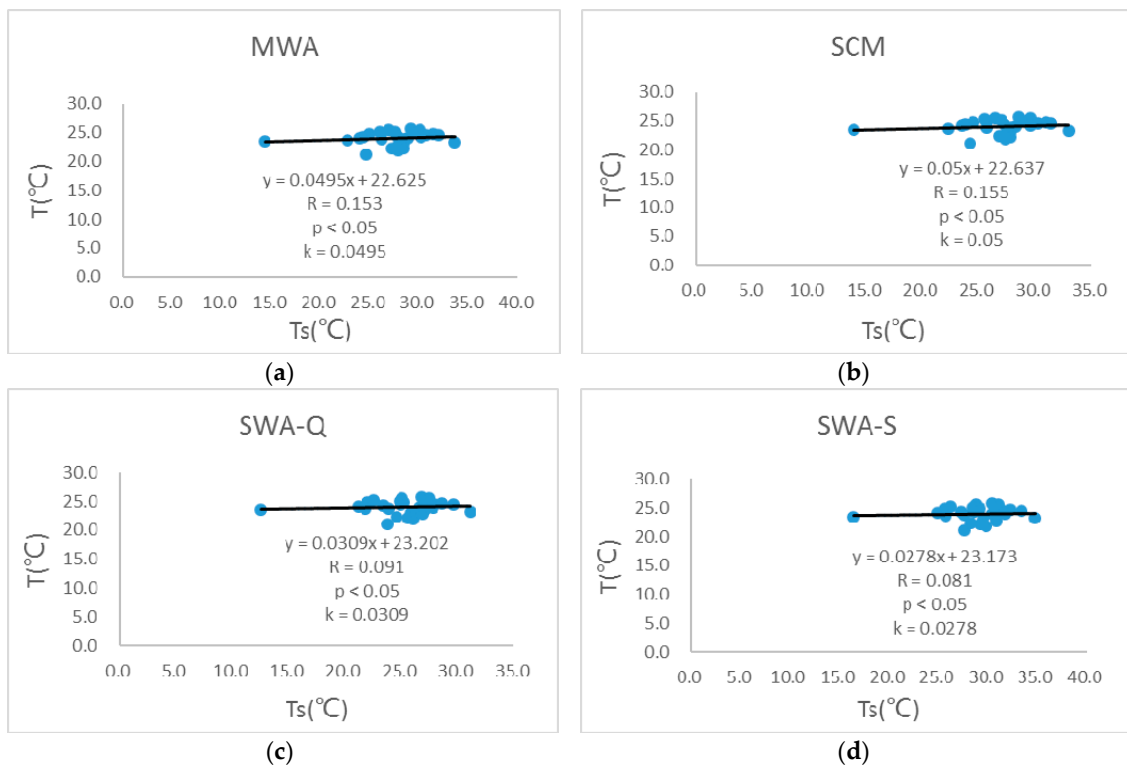


Figure 5. The scatterplots of the LST retrievals by the (a) MWA; (b) SCM; (c) SWA-Q; and (d) SWA-S compared with the mean daily air temperature in 18 October 2015.

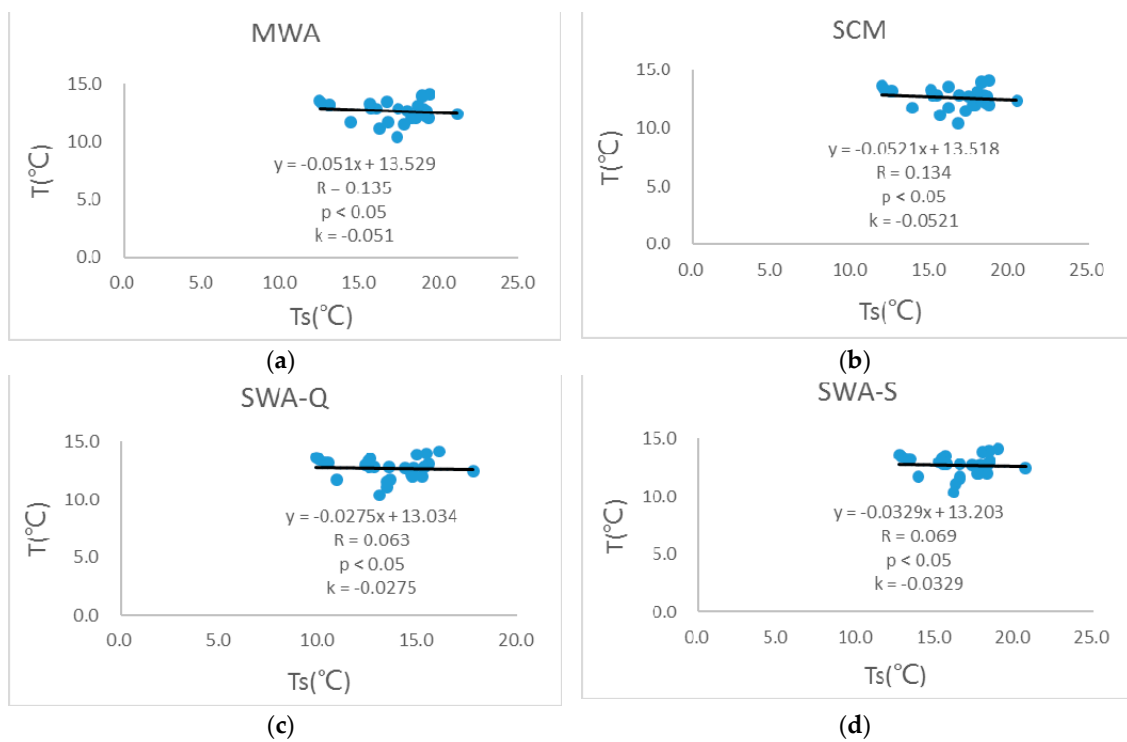


Figure 6. The scatter-plots of the LST retrieval by the (a) MWA; (b) SCM; (c) SWA-Q; and (d) SWA-S compared with the mean daily air temperature in 7 February 2016.

Figure 6 shows that the distribution of LST retrieval is more scattered than that of the mean daily air temperature. In addition, the range of the SWA-Q's LST retrieval, basically between 9.0 °C and 18.0 °C, is relatively closer to the range of measured mean air temperature, approximately between 10.0 °C and 14.0 °C, compared with the range of the other three methods' LST retrievals, mostly between 12.0 °C and 21.0 °C.

For comparing the precision of four methods in a more precise and quantitative way, two statistical indices, the root mean square error (RMSE) and mean bias error (MBE), are used to assess the deviation between the estimators and observed values, and calculated as Equations (31) and (32) [23,32]:

$$RMSE = \sqrt{\frac{\sum_{i=1}^n (x_i - y_i)^2}{n}} \quad (31)$$

$$MBE = \frac{\sum_{i=1}^n (x_i - y_i)}{n} \quad (32)$$

where *RMSE* is the root mean square error between variable *x* and *y*; *MBE* is the mean bias error between variable *x* and *y*; and *x* and *y* are, respectively, the LST retrievals by four methods and observed mean daily air temperature in this paper.

In Table 8, the correlation coefficients are relatively low, in general, which means the correlation between the LST retrieval of fixed points and observed air temperature is relatively low, which may be because the measured LST data are not found, and the observed air temperature which is approximately utilized as the LST in this paper has relatively weak correlation with the LST retrieval. Additionally, the SWA-Q's RMSEs and MBEs are less than the other three methods, which means the SWA-Q's precision is higher than the other three methods. Furthermore, according to the RMSE and MBE of the SWA-Q, the accuracy of the LST retrieval on 7 February 2016 is the highest, followed by that on 29 November 2013 and 16 November 2014, and that on 18 October 2015 is the lowest. Therefore, the LST retrieval of the SWA-Q is more accurate than the LST retrievals of the other three methods. For this reason, the LST retrieval of the SWA-Q is applied to analyze the LST and UHI in Shenzhen and Hong Kong from 2013 to 2016.

Table 8. Accuracy comparison of four methods in 2013 and 2016.

Date	Method	R	RMSE	MBE
29 November 2013	MWA	0.020	4.74	3.87
	SCM	0.018	4.50	3.61
	SWA-Q	0.013	3.05	1.76
	SWA-S	0.082	5.39	4.79
16 November 2014	MWA	0.080	4.83	4.52
	SCM	0.080	4.03	3.63
	SWA-Q	0.072	3.40	2.69
	SWA-S	0.073	6.78	6.52
18 October 2015	MWA	0.153	4.84	3.44
	SCM	0.155	4.49	2.95
	SWA-Q	0.091	3.64	1.31
	SWA-S	0.081	6.05	5.09
7 February 2016	MWA	0.135	4.96	4.36
	SCM	0.134	4.47	3.80
	SWA-Q	0.063	2.30	0.88
	SWA-S	0.069	4.37	3.86

According to the accuracy analysis result, the accuracy of the four methods is uneven, so the error analysis is illuminated in three aspects, namely, data, methodology, and study area.

The data's error analysis is generalized in three points. Firstly, although the satellite images have no obvious cloud cover in the study areas of this paper, a certain amount of water vapor still influence the accuracy of the LST conversion. Secondly, the atmospheric correction is not executed in the image pre-processing of this study, so the radiance error caused by the atmospheric scattering of the satellite images is not eliminated. Thirdly, because the measured LST data in the study areas are not found, the observed air temperature that already exists contains a certain amount of error, and the actual LST at the time of the images is approximately utilized as the LST in this paper.

The methodology's error analysis is summarized in two points. Firstly, Shenzhen and Hong Kong are located in a subtropical area, but the standard profile for subtropical areas is not found, so the standard profiles for tropical areas or the global scale are adopted, which may cause a certain amount of deviation. For example, the standard atmosphere for tropical areas is applied in the calculation of mean atmospheric temperature and the 1976 US standard is utilized in the computation of atmospheric transmittance, etc. [16,29]. Secondly, some related databases for Landsat 8 are not found, so some other related databases are employed which may also cause a certain amount of deviation. For instance, the calculation of land surface emissivity, atmospheric functions in the SCM, and coefficients in the SWA-S are, respectively, based on the ASTER spectral database, GAPRI database, and MAPRI database [27,28].

Remote sensing is more applicable to large-scale areas, while the study areas in this paper, Shenzhen and Hong Kong, whose total area is approximate 3102 km², are not large-scale areas for remote sensing and, therefore, the scale of the study area may affect the accuracy of this study [32,34].

4.2. Land Surface Temperature Distribution

As mentioned above, the SWA-Q is the most accurate method among the four methods, so the LST retrieval of the SWA-Q is employed to export the LST and UHI distribution maps with ArcGIS 10.1 (Figures 7 and 8) and analyze the LST and UHI in Shenzhen and Hong Kong from 2013 to 2016.

In Figure 7, the green area means that the LST in that area is lower than the mean LST. In Shenzhen, the high-LST zones, namely, the red area in Figure 7, mainly concentrate on the west of Shenzhen, including Guangming District, Baoan District, and Longhua District. The high-LST zones in Hong Kong mostly concentrate on Yuen Long, the west coast of Hong Kong, and Chulocock Island (namely, Hong Kong International Airport, located in the north of Lantau Island). In addition, the high-LST zones in 2015 are obviously larger than that in other years, which may be because the temperature difference in 2015 is larger than that in the other years. According to the measured air temperature, the temperature difference in 2015 is about 5 °C, while the temperature difference is around 3 °C in 2014 and 4 °C in 2013 and 2016. Additionally, the high-LST zones are relatively dispersive in 2013 and 2014, but relatively concentrative in 2015 and 2016.

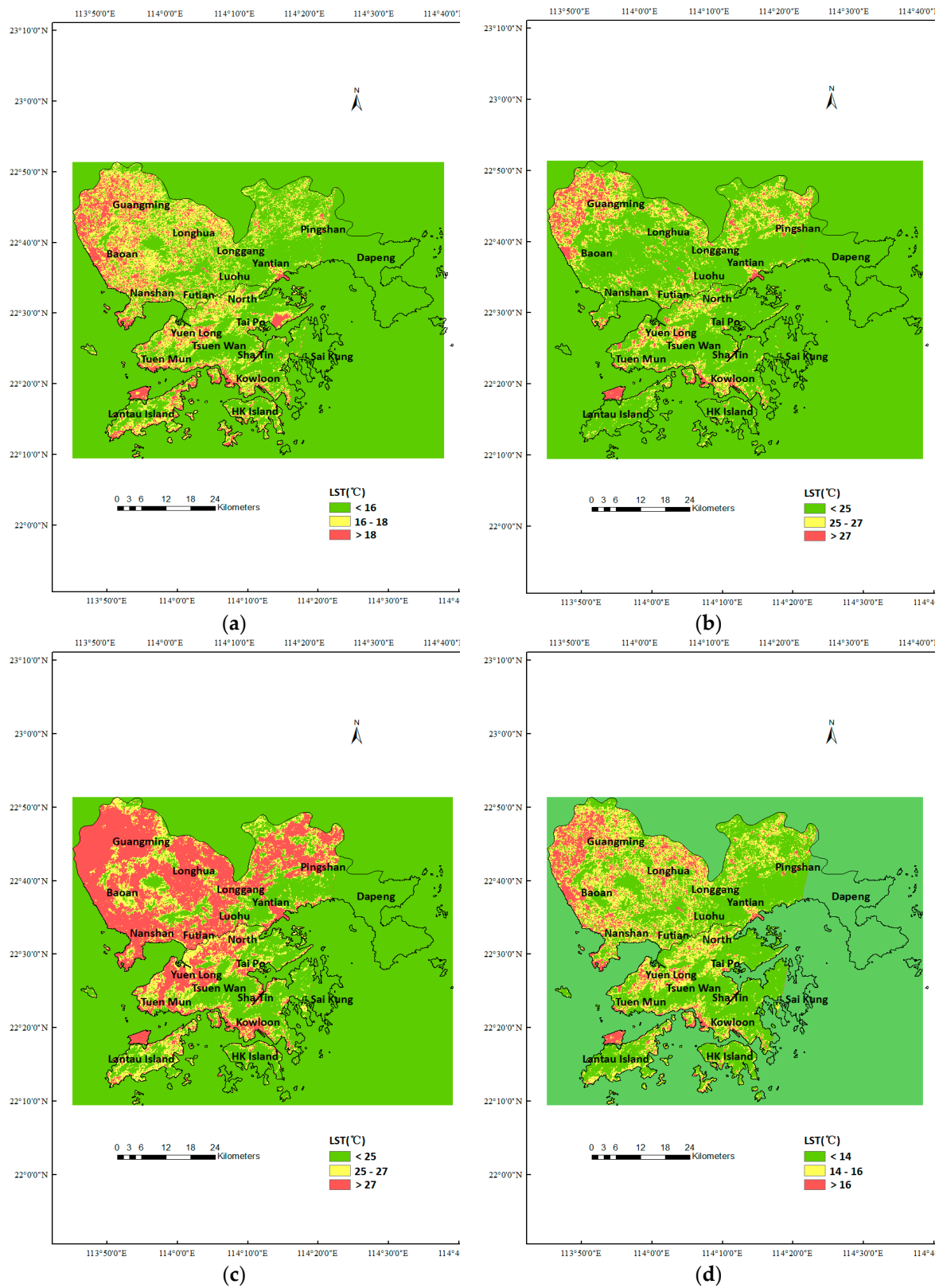


Figure 7. The LST distribution in Shenzhen and Hong Kong in (a) November 2013; (b) November 2014; (c) October 2015 and (d) February 2016.

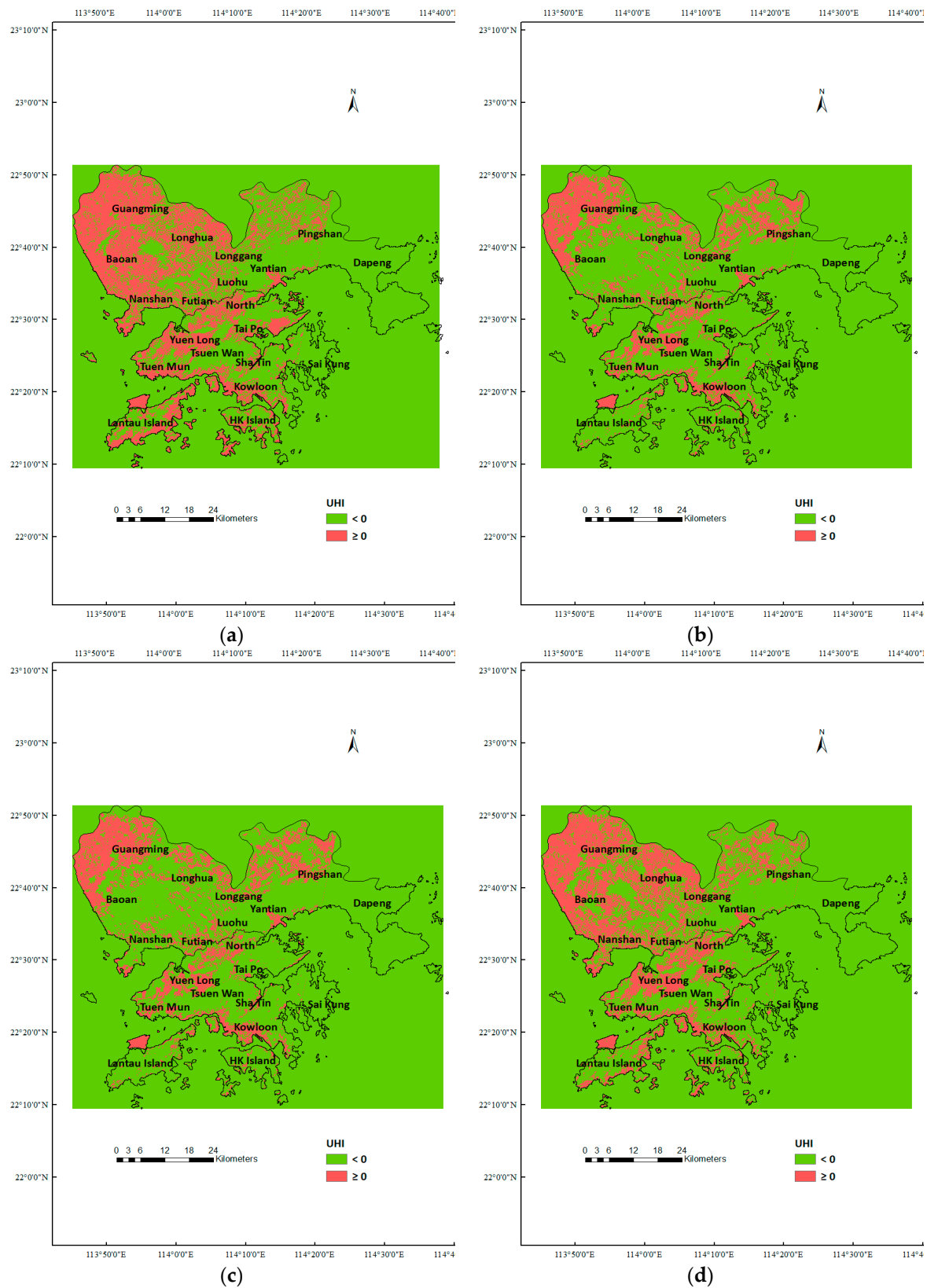


Figure 8. The UHI distribution in Shenzhen and Hong Kong in (a) November 2013; (b) November 2014; (c) October 2015; and (d) February 2016.

The difference vegetation index (DVI) is utilized to extrapolate the atmospheric particulate pollution and calculated as Equation (33) [14]:

$$DVI = NIR - R \tag{33}$$

where *DVI* is the difference vegetation index; *NIR* is the near-infrared band; and *R* is the red band.

For learning more about the relationship among the LST, NDVI, and DVI, the correlation coefficients with LST are presented in Table 9. The correlation coefficients between the LST and NDVI are negative in 2014 and 2015, but positive in 2013 and 2016, that is to say, the LST and NDVI has no explicit relationship. Additionally, the correlation between the LST and DVI is slightly positive; in other words, the higher LST is slightly related to the higher atmospheric particulate concentration [14].

Table 9. The correlation coefficients with LST.

Date	NDVI	DVI
29 November 2013	0.74	0.40
16 November 2014	−0.92	0.42
18 October 2015	−0.91	0.49
7 February 2016	0.95	0.37

The high NDVI is mainly located in Yantian, Tsuen Wan, and Lantau Island in 2013 and 2015, but mostly located in Guangming, Longhua, and Chulocock Island in 2014 and 2016; that is to say, the distribution of high NDVI is unfixed from 2013 to 2016 (Figure 9). However, the high DVI is mainly located in Yantian, North, Tsuen Wan, and Lantau Island, in other words, the distribution of high DVI is relatively stationary from 2013 to 2016 (Figure 10).

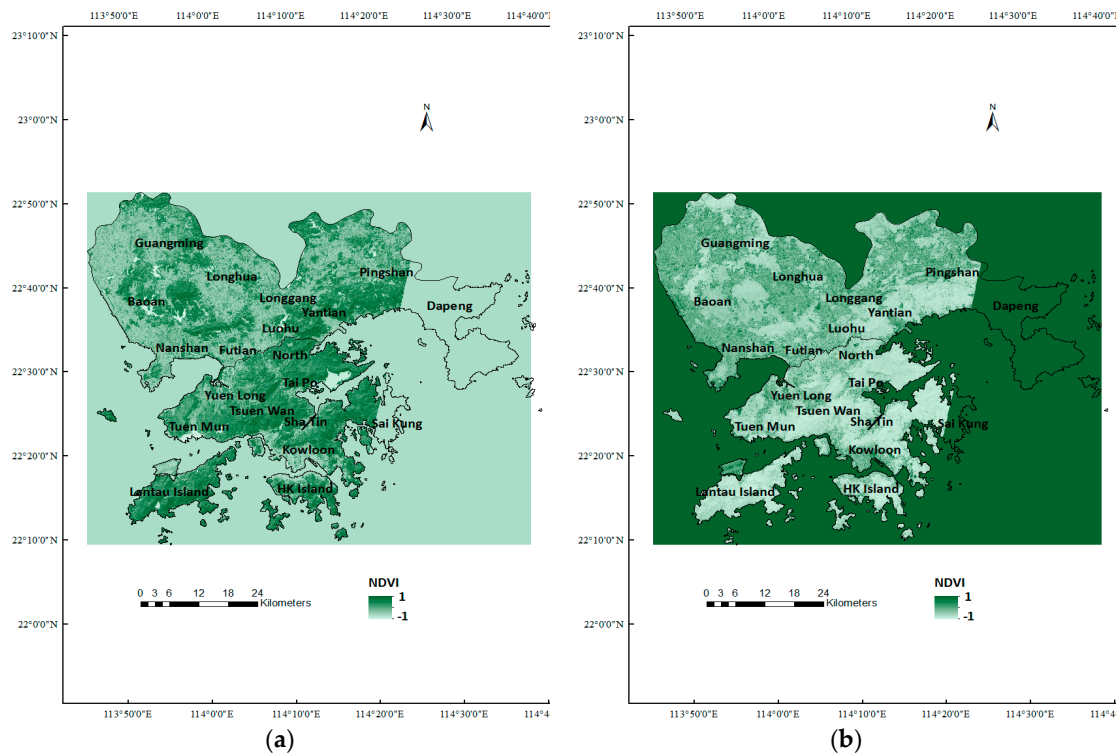


Figure 9. Cont.

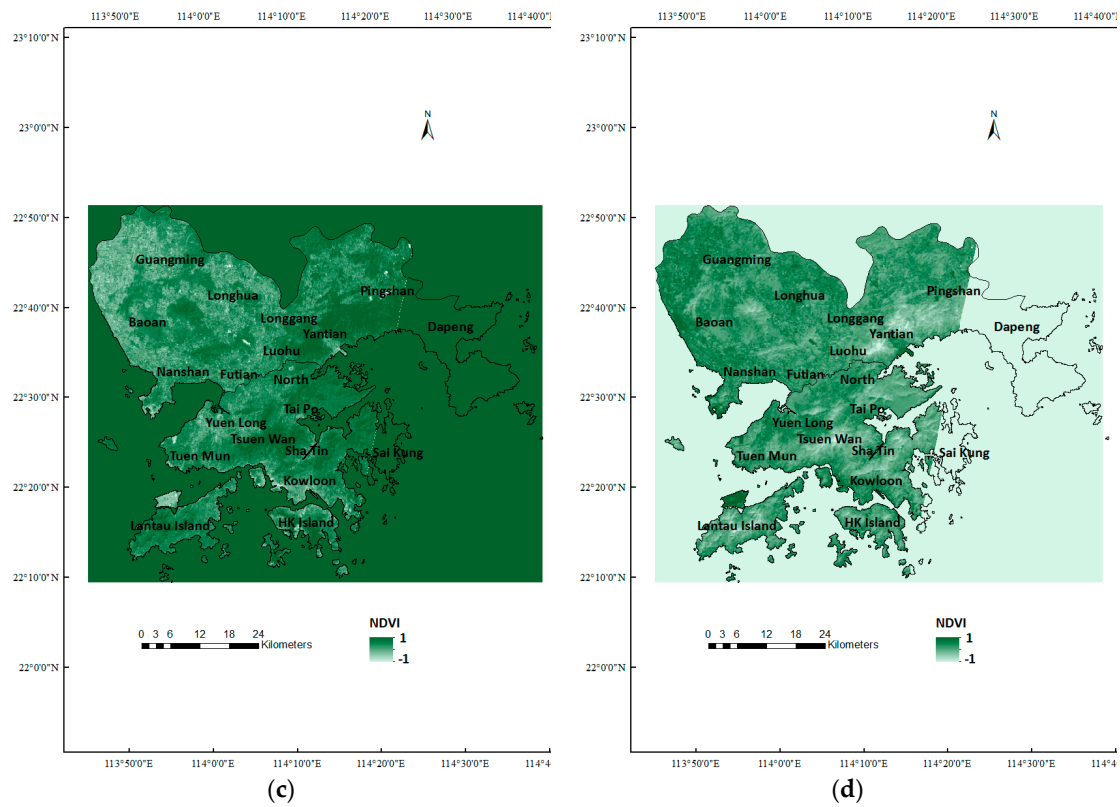


Figure 9. The NDVI distribution in Shenzhen and Hong Kong in (a) November 2013; (b) November 2014; (c) October 2015; and (d) February 2016.

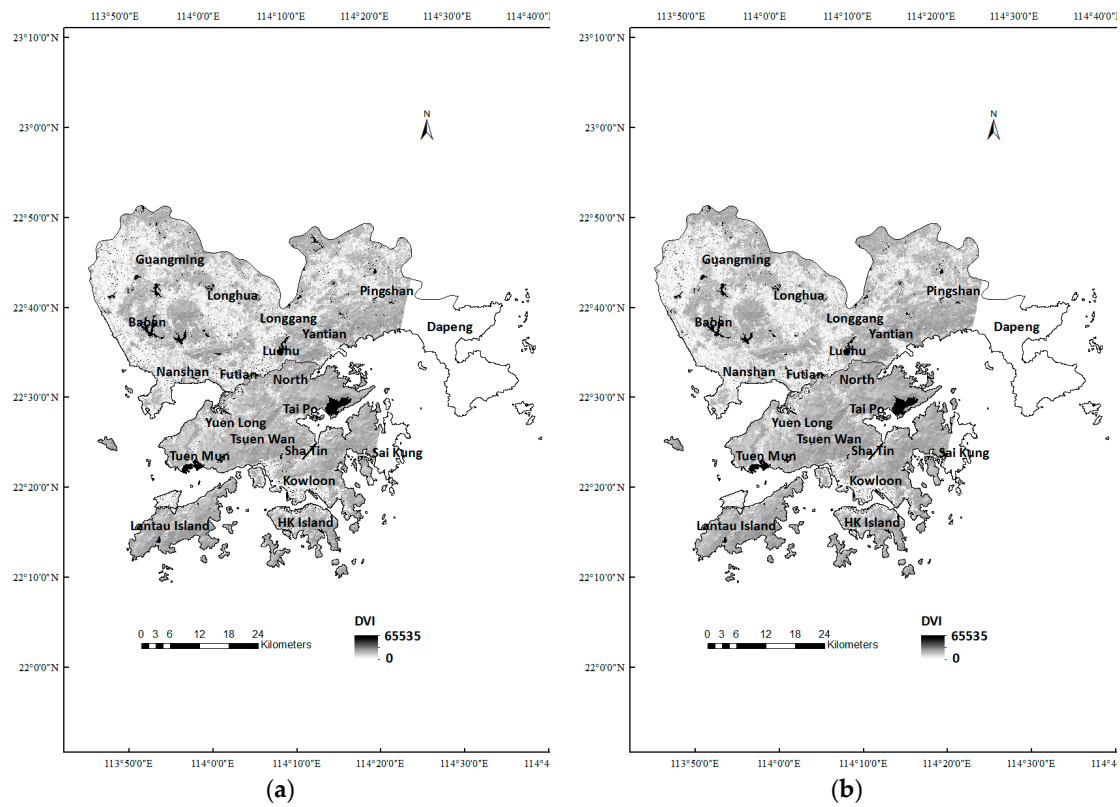


Figure 10. Cont.

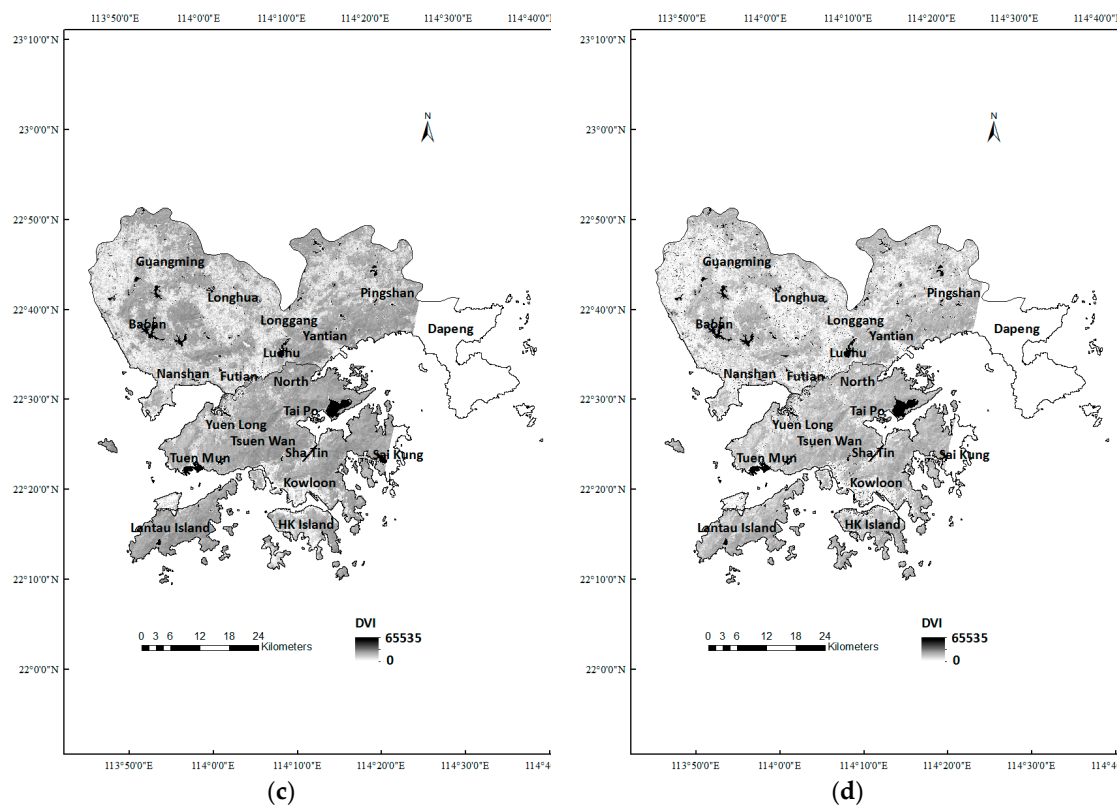


Figure 10. The DVI distribution in Shenzhen and Hong Kong in (a) November 2013; (b) November 2014; (c) October 2015; and (d) February 2016.

4.3. Urban Heat Island Assessment

The UHI intensity is estimated by the relative LST as Equation (34) (Table 10) [14]:

$$T_r = \frac{T_s - \bar{T}_s}{\bar{T}_s} \quad (34)$$

where T_r is the relative LST; T_s is the LST (K); \bar{T}_s and \bar{T}_s is the mean LST (K).

Table 10. The classification of UHI intensity.

Relative LST	UHI Intensity
<0	Urban heat sink
≥0	UHI

According to the calculation result, the relative LST in both Shenzhen and Hong Kong is lower than 0.1, which means the UHI intensity in Shenzhen and Hong Kong is weak, in other words, Shenzhen and Hong Kong are weak UHI regions. Compare Figure 7 with Figure 10, the UHI in Shenzhen and Hong Kong approximate to the high-LST zones. Furthermore, the proportion of UHI in Shenzhen and Hong Kong from 2013 to 2016 extracted from Figure 10 with ENVI 5.1 is presented in Table 11. The proportion of UHI is high in 2013 and 2016 when the correlation between LST and NDVI is positive, but low in 2014 and 2015 when the correlation between LST and NDVI is negative, that is to say, the growth condition rather than the distribution of vegetation may impact the distribution of UHI. The proportion of UHI in Shenzhen is always higher than that in Hong Kong from 2013 to 2016, in other words, the UHI-affected area in Shenzhen is larger than that in Hong Kong.

Table 11. The proportion of UHI in Shenzhen and Hong Kong from 2013 to 2016.

Cities	UHI (%)			
	29 November 2013	16 November 2014	18 October 2015	7 February 2016
SZ & HK	18.7	10.8	10.8	15.8
Shenzhen	18.6	11.6	11.6	17.1
Hong Kong	16.6	8.2	8.2	11.8

5. Discussion

In terms of LST estimation, Liu and Zhang estimated the LST in Hong Kong via the MWA using Landsat TM and ASTER data and found that the LST retrieval using Landsat TM data, whose overall accuracy was 0.7 °C, was more accurate [17]. Xie et al. converted the LST in Shenzhen, China by the SCM using Landsat 5 TM data [22]. Wong et al. derived the LST in Hong Kong using the Chinese small satellite HJ-1B data [41]. In this paper, four methods, namely, the MWA, SCM, SWA-Q, and SWA-S, and newer satellite data, namely, Landsat 8 data, are adopted to derive the LST in Shenzhen and Hong Kong. The LST retrieval using the SWA-Q on 7 February 2016 is the most precise LST retrieval in this paper whose RMSE and MBE are, respectively, 2.30 °C and 0.88 °C, and whose accuracy is close to Liu and Zhang's study [17]. Additionally, the LST's data of the 28 weather stations are extracted to compare with the observed air temperature, and then compared the accuracy of the four methods mentioned above. In addition, Liu and Zhang discovered that the correlation coefficient between LST and NDVI was weakly negative [17] and Xie et al. indicated that the LST had negative correlation with the vegetation fraction and positive correlation with the impervious surface area [22]; however, in this paper, the LST and NDVI had no noticeable relationship. Furthermore, the higher LST is correlated to the higher atmospheric particulate concentration in Shenzhen and Hong Kong.

In terms of the UHI assessment, Memon et al. and Siu et al., respectively, utilized the meteorology data from the Hong Kong Observatory to judge the UHI intensity in Hong Kong which just exerted the dotted data rather than the surface data to evaluate the UHI intensity [38,42,43]. Liu et al., Xie et al., and Wong et al., respectively, estimated the UHI intensity in Shenzhen or Hong Kong using satellite data just like this paper [17,22,41]. However, the assessments of UHI intensity have noticeable differences. Liu and Zhang evaluated that most areas in Hong Kong were the strongest UHI areas [17]; on the contrary, in this study, the UHI intensity is weak in both Shenzhen and Hong Kong. Furthermore, few studies compared the UHI conditions between Shenzhen and Hong Kong. In this study, the growth condition of vegetation may impact the distribution of UHI, and the UHI-affected area in Shenzhen is larger than that in Hong Kong from 2013 to 2016. Additionally, the deficiency of this study is that the satellite images cannot cover the whole study area and the areas without data are mainly located in Dapeng District, Shenzhen, and Tai Po and Sai Kung, Hong Kong.

6. Conclusions

Under the background of global warming and urbanization, the study of UHI attracts widespread attention today, and with the rapid development of satellite technology, satellite images, which can acquire surface data rather than dotted data, compared with the traditional method, like meteorology data utilization, have become more and more popular recently. In this paper, the LST of Shenzhen and Hong Kong is retrieved by four methods, namely the MWA, SCM, SWA-Q, and SWA-S, using the Landsat 8 data from 29 November 2013, 16 November 2014, 18 October 2015, and 7 February 2016. Then, after the accuracy analysis, the SWA-Q is estimated as the most accurate method among the four methods mentioned above and, therefore, the LST retrievals by SWA-Q are applied to analyze the LST distribution and UHI intensity in Shenzhen and Hong Kong from 2013 to 2016. From 2013 to 2016, the high-LST zones or UHIs in Shenzhen and Hong Kong are substantially identical, mainly in Longhua, Baoan, and Guangming of Shenzhen, and in Yuen Long, the west coast of Hong Kong, and Chulocock Island, Hong Kong. Additionally, the high-LST zones are relatively dispersive in 2013 and

2014, but relatively concentrative in 2015 and 2016. Although the LST has not obviously correlated with the vegetation distribution, the growth condition of vegetation may impact the distribution of UHI, and the high LST is slightly correlated to the high atmospheric particulate concentration. Furthermore, in general, Shenzhen and Hong Kong are weak UHI regions and the UHI-affected area in Shenzhen is larger than that in Hong Kong from 2013 to 2016.

Acknowledgments: The data from the website of USGS and from the local government of Hong Kong and Shenzhen are highly appreciated. This research is partially supported by the National Key Research and Development Program of China (Project Ref. No. 2016YFB0501501).

Author Contributions: Jinyeu Tsou and Jing Zhuang conceived and designed the experiments; Jing Zhuang performed the experiments; Yu Li analyzed the data; Jinyeu Tsou contributed reagents/materials/analysis tools; Yuanzhi Zhang and Yu Li wrote the paper.

Conflicts of Interest: The authors declare no conflict of interest.

References

1. Kleerekoper, L.; van Esch, M.; Salcedo, T.B. How to make a city climate-proof, addressing the urban heat island effect. *Resour. Conserv. Recycl.* **2012**, *64*, 30–38. [[CrossRef](#)]
2. Nakayama, T.; Hashimoto, S. Analysis of the ability of water resources to reduce the urban heat island in the Tokyo megalopolis. *Environ. Pollut.* **2011**, *159*, 2164–2173. [[CrossRef](#)] [[PubMed](#)]
3. Emmanuel, R.; Krüger, E. Urban heat island and its impact on climate change resilience in a shrinking city: The case of Glasgow, UK. *Build. Environ.* **2012**, *53*, 137–149. [[CrossRef](#)]
4. Li, W.; Wang, Y.; Peng, J.; Li, G. Landscape spatial changes associated with rapid urbanization in Shenzhen, China. *Int. J. Sustain. Dev. World Ecol.* **2005**, *12*, 314–325. [[CrossRef](#)]
5. Wong, J.K.W.; Lau, L.S.-K. From the ‘urban heat island’ to the ‘green island’? A preliminary investigation into the potential of retrofitting green roofs in Mongkok district of Hong Kong. *Habitat Int.* **2013**, *39*, 25–35. [[CrossRef](#)]
6. Kukla, G.; Gavin, J.; Karl, T. Urban warming. *J. Appl. Meteorol.* **1986**, *25*, 1265–1270. [[CrossRef](#)]
7. Tomlinson, C.J.; Chapman, L.; Thornes, J.E.; Baker, C.J. Derivation of Birmingham’s summer surface urban heat island from MODIS satellite images. *Int. J. Climatol.* **2012**, *32*, 214–224. [[CrossRef](#)]
8. Rao, P.K. Remote Sensing of Urban Heat Islands from an Environmental Satellite. *Bull. Am. Meteorol. Soc.* **1972**, *53*, 647–648.
9. Pan, J. Area Delineation and Spatial-Temporal Dynamics of Urban Heat Island in Lanzhou City, China Using Remote Sensing Imagery. *J. Indian Soc. Remote Sens.* **2015**, *44*, 111–127. [[CrossRef](#)]
10. Howard, L. *The Climate of London Deduced from Meteorological Observations Made in the Metropolis and at Various Places around It*; Harvey and Darton: London, UK, 1833; Volume 1, p. 348.
11. Zinzi, M. Cool materials and cool roofs: Potentialities in Mediterranean buildings. *Adv. Build. Energy Res.* **2010**, *4*, 201–266. [[CrossRef](#)]
12. Weng, Q.; Yang, S. Managing the adverse thermal effects of urban development in a densely populated Chinese city. *J. Environ. Manag.* **2004**, *70*, 145–156. [[CrossRef](#)]
13. Rinner, C.; Hussain, M. Toronto’s Urban Heat Island—Exploring the Relationship between Land Use and Surface Temperature. *Remote Sens.* **2011**, *3*, 1251–1265. [[CrossRef](#)]
14. Xu, L.Y.; Xie, X.D.; Li, S. Correlation analysis of the urban heat island effect and the spatial and temporal distribution of atmospheric particulates using TM images in Beijing. *Environ. Pollut.* **2013**, *178*, 102–114. [[CrossRef](#)] [[PubMed](#)]
15. Choi, Y.-Y.; Suh, M.-S.; Park, K.-H. Assessment of Surface Urban Heat Islands over Three Megacities in East Asia Using Land Surface Temperature Data Retrieved from COMS. *Remote Sens.* **2014**, *6*, 5852–5867. [[CrossRef](#)]
16. Qin, Z.; Karnieli, A.; Berliner, P. A mono-window algorithm for retrieving land surface temperature from Landsat TM data and its application to the Israel-Egypt border region. *Int. J. Remote Sens.* **2001**, *22*, 3719–3746. [[CrossRef](#)]
17. Liu, L.; Zhang, Y. Urban Heat Island Analysis Using the Landsat TM Data and ASTER Data: A Case Study in Hong Kong. *Remote Sens.* **2011**, *3*, 1535–1552. [[CrossRef](#)]

18. Wang, F.; Qin, Z.; Song, C.; Tu, L.; Karnieli, A.; Zhao, S. An Improved Mono-Window Algorithm for Land Surface Temperature Retrieval from Landsat 8 Thermal Infrared Sensor Data. *Remote Sens.* **2015**, *7*, 4268–4289. [[CrossRef](#)]
19. Zhang, Y.; Chen, L.; Wang, Y.; Chen, L.; Yao, F.; Wu, P.; Wang, B.; Li, Y.; Zhou, T.; Zhang, T. Research on the Contribution of Urban Land Surface Moisture to the Alleviation Effect of Urban Land Surface Heat Based on Landsat 8 Data. *Remote Sens.* **2015**, *7*, 10737–10762. [[CrossRef](#)]
20. Jiménez-Muñoz, J.C.; Sobrino, J.A. A generalized single-channel method for retrieving land surface temperature from remote sensing data. *J. Geophys. Res.* **2003**, *108*. [[CrossRef](#)]
21. Jimenez-Munoz, J.C.; Cristobal, J.; Sobrino, J.A.; Soria, G.; Ninyerola, M.; Pons, X.; Pons, X. Revision of the Single-Channel Algorithm for Land Surface Temperature Retrieval From Landsat Thermal-Infrared Data. *IEEE Trans. Geosci. Remote Sens.* **2009**, *47*, 339–349. [[CrossRef](#)]
22. Xie, M.; Wang, Y.; Chang, Q.; Fu, M.; Ye, M. Assessment of landscape patterns affecting land surface temperature in different biophysical gradients in Shenzhen, China. *Urban Ecosyst.* **2013**, *16*, 871–886. [[CrossRef](#)]
23. Zhang, Z.; He, G.; Wang, M.; Long, T.; Wang, G.; Zhang, X.; Jiao, W. Towards an operational method for land surface temperature retrieval from Landsat 8 data. *Remote Sens. Lett.* **2016**, *7*, 279–288. [[CrossRef](#)]
24. Qin, Z.; Dall’Olmo, G.; Karnieli, A.; Berliner, P. Derivation of split window algorithm and its sensitivity analysis for retrieving land surface temperature from NOAA-advanced very high resolution radiometer data. *J. Geophys. Res. Atmos.* **2001**, *106*, 22655–22670. [[CrossRef](#)]
25. Jimenez-Munoz, J.-C.; Sobrino, J.A. Split-Window Coefficients for Land Surface Temperature Retrieval from Low-Resolution Thermal Infrared Sensors. *IEEE Geosci. Remote Sens. Lett.* **2008**, *5*, 806–809. [[CrossRef](#)]
26. Rozenstein, O.; Qin, Z.; Derimian, Y.; Karnieli, A. Derivation of land surface temperature for Landsat-8 TIRS using a split window algorithm. *Sensors* **2014**, *14*, 5768–5780. [[CrossRef](#)] [[PubMed](#)]
27. Jin, M.; Li, J.; Wang, C.; Shang, R. A Practical Split-Window Algorithm for Retrieving Land Surface Temperature from Landsat-8 Data and a Case Study of an Urban Area in China. *Remote Sens.* **2015**, *7*, 4371–4390. [[CrossRef](#)]
28. Jimenez-Munoz, J.C.; Sobrino, J.A.; Skokovic, D.; Mattar, C.; Cristobal, J. Land Surface Temperature Retrieval Methods from Landsat-8 Thermal Infrared Sensor Data. *IEEE Geosci. Remote Sens. Lett.* **2014**, *11*, 1840–1843. [[CrossRef](#)]
29. Yu, X.; Guo, X.; Wu, Z. Land Surface Temperature Retrieval from Landsat 8 TIRS—Comparison between Radiative Transfer Equation-Based Method, Split Window Algorithm and Single Channel Method. *Remote Sens.* **2014**, *6*, 9829–9852. [[CrossRef](#)]
30. Du, C.; Ren, H.; Qin, Q.; Meng, J.; Zhao, S. A Practical Split-Window Algorithm for Estimating Land Surface Temperature from Landsat 8 Data. *Remote Sens.* **2015**, *7*, 647–665. [[CrossRef](#)]
31. Google Maps. Available online: <https://www.google.com.hk/maps/@22.352734,114.1277,11z> (accessed on 9 April 2016).
32. Wikipedia. Available online: https://en.wikipedia.org/wiki/Main_Page (accessed on 30 May 2016).
33. Census and Statistics Department. Available online: <http://www.censtatd.gov.hk/> (accessed on 8 April 2016).
34. Planning Department. Available online: <http://www.pland.gov.hk/> (accessed on 9 April 2016).
35. United States Geological Survey. Available online: <http://glavis.usgs.gov/> (accessed on 21 April 2016).
36. DIVA-GIS. Available online: <http://www.diva-gis.org/download> (accessed on 27 April 2016).
37. Weather Website. Available online: <https://www.tianqi.com> (accessed on 1 August 2016).
38. Hong Kong Observatory. Available online: http://www.weather.gov.hk/cis/climat_e.htm (accessed on 1 April 2016).
39. Leuning, R.; Kelliher, F.M.; Pury, D.G.G.; Schulze, E.D. Leaf nitrogen, photosynthesis, conductance and transpiration: Scaling from leaves to canopies. *Plant Cell Environ* **1995**, *18*, 1183–1200. [[CrossRef](#)]
40. Sobrino, J.A.; Jimenez Muoz, J.C.; Soria, G.; Romaguera, M.; Guanter, L.; Moreno, J.; Plaza, A.; Martinez, P. Land Surface Emissivity Retrieval from Different VNIR and TIR Sensors. *IEEE Trans. Geosci. Remote Sens.* **2008**, *46*, 316–327. [[CrossRef](#)]
41. Wong, M.S.; Yang, J.; Nichol, J.; Weng, Q.; Menenti, M.; Chan, P.W. Modeling of Anthropogenic Heat Flux Using HJ-1B Chinese Small Satellite Image: A Study of Heterogeneous Urbanized Areas in Hong Kong. *IEEE Geosci. Remote Sens. Lett.* **2015**, *12*, 1466–1470. [[CrossRef](#)]

42. Memon, R.A.; Leung, D.Y.C.; Liu, C.-H.; Leung, M.K.H. Urban heat island and its effect on the cooling and heating demands in urban and suburban areas of Hong Kong. *Theor. Appl. Climatol.* **2010**, *103*, 441–450. [[CrossRef](#)]
43. Siu, L.W.; Hart, M.A. Quantifying urban heat island intensity in Hong Kong SAR, China. *Environ. Monit. Assess.* **2013**, *185*, 4383–4398. [[CrossRef](#)] [[PubMed](#)]



© 2017 by the authors. Licensee MDPI, Basel, Switzerland. This article is an open access article distributed under the terms and conditions of the Creative Commons Attribution (CC BY) license (<http://creativecommons.org/licenses/by/4.0/>).